Journal of Nuclear Materials 430 (2012) 171–180

Contents lists available at SciVerse ScienceDirect

Journal of Nuclear Materials

journal homepage: www.elsevier.com/locate/jnucmat

EFTEM and EELS analysis of the oxide layer formed on HCM12A exposed to SCW

Jeremy Bischoff *, Arthur T. Motta

Department of Mechanical and Nuclear Engineering, Pennsylvania State University, 227 Reber Building, University Park, PA 16802, USA

ARTICLE INFO

Article history:
Received 23 December 2011
Accepted 12 June 2012
Available online 20 June 2012

ABSTRACT

The inner-diffusion layer interface of an HCM12A sample oxidized in 600 °C supercritical water (SCW) was analyzed using EFTEM and EELS. The EFTEM analysis showed the presence of chromium-rich zones linked with the porosity within the inner layer, as well as a nanometric iron–chromium separation, which may be linked with the presence of both Fe_3O_4 and $FeCr_2O_4$ in this layer. The diffusion layer was characterized by large chromium-rich oxides located at the tempered martensite lath boundaries, which suggested the preferential grain boundary diffusion of oxygen and the preferential oxidation of the chromium carbides present at these boundaries. The metal grains of the diffusion layer contained nanometric chromium-rich spinel oxides. The presence of large chromium-rich oxide precipitates in the diffusion layer appears to help improve the corrosion resistance of these alloys.

1. Introduction

1.1. Background

As part of the Generation IV forum, the Supercritical Water Reactor is envisioned for its high thermal efficiency and simplified core [1] and is designed to operate at high outlet temperature (between 500 °C and 600 °C). Consequently, the goal is to find cladding and structural materials that can perform at these elevated temperatures for extended exposures. Because of their resistance to irradiation and stress corrosion cracking, ferritic–martensitic steels, such as HCM12A, are candidate materials for the supercritical water reactor [2]. Nevertheless, the process of uniform corrosion of HCM12A has to be better understood in order to better predict and control it.

The oxide layers formed on HCM12A during exposure to supercritical water have been previously studied using scanning electron microscopy (SEM), X-ray diffraction (XRD), and electron backscatter diffraction (EBSD) [2–4]. These studies have shown that HCM12A forms a dual layer structure at 500 °C with Fe_3O_4 in the outer layer and spinel $(Fe,Cr)_3O_4$ in the inner layer with some evidence of Cr_2O_3 [4]. At 600 °C a diffusion layer is also observed, containing a mixture of oxide precipitates and metal grains [2].

The present article follows a previous experiment, which analyzed the oxide layer microstructure of HCM12A using microbeam synchrotron radiation diffraction and fluorescence, and studied the influence of the base alloy microstructure on the advancement of the oxide front using energy filtered transmission electron microscopy (EFTEM) [5]. That study showed that the carbides present at the tempered martensite lath boundaries were oxidized preferentially, leading to the formation of chromium-rich oxide precipitates along these boundaries in the diffusion layer [5]. The present article shows a more detailed analysis of the inner and diffusion layers of an HCM12A sample exposed to 600 °C for 2 weeks in supercritical water (SCW), using EFTEM and electron energy-loss spectroscopy (EELS) in order to better understand the advancement of the inner layer into the diffusion layer. The focus is to obtain a micrometric and nanometric distribution of elements in these two layers as well as their oxide microstructure.

1.2. Previous EELS characterization of iron oxides

Several EELS studies have been performed on iron oxides, showing differences in the EELS spectra from FeO, Fe_3O_4 and Fe_2O_3 [6–10]. The study of both the oxygen and the iron edges can generate information on the oxide phase being analyzed. Since it is difficult to distinguish between the various iron oxide phases using only the iron edge, we focused our analysis on the oxygen edge, which also gives information on the oxidation state of iron and the iron oxide phase the oxygen atoms belong to. Colliex et al. have studied the iron oxides using EELS [6].

Fig. 1 shows the variations of the oxygen edge spectrum corresponding to the different iron oxide phases [6]. The oxygen edge contains four main peaks referred to as (a–d) (marked in the α-Fe_2O_3 quadrant) in Fig. 1. The relative height and position of these peaks give information on the electronic structure and coordination chemistry of the absorbing O atoms and can also help measure the valence state of iron, the average interatomic distances between the absorbing O atom and its nearest neighbors,

* Corresponding author. Tel.: +1 814 865 0036.
E-mail address: bischoff.jeremy@gmail.com (J. Bischoff).

0022-3115/$ - see front matter © 2012 Elsevier B.V. All rights reserved.
http://dx.doi.org/10.1016/j.jnucmat.2012.06.017

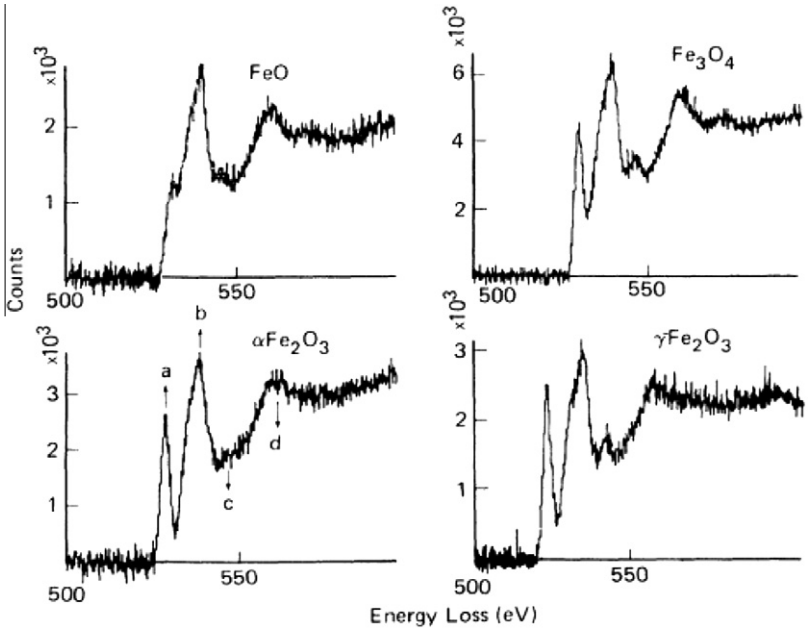

Fig. 1. EELS oxygen edge spectra for the different iron oxides: FeO, Fe_3O_4, γ-Fe_2O_3 and α-Fe_2O_3 [6].

the relative covalency of the Fe—O bond and the coordination number. The pre-peak (a) results from the transition of an electron from the O 1*s* shell to the unoccupied hybridized O 2p/Fe 3d states. As a result the intensity of this peak determines the number of unoccupied 3d states from the Fe atoms bonding with the absorbing O atom, thus indirectly measuring the valence state of the iron atoms [6]. The intensity of this peak is higher in FeO than in Fe_2O_3 due to the decrease of the fraction of Fe^{2+}. More Fe^{2+} means more electrons in the hybridized O 2p/Fe 3d orbitals and therefore less unoccupied states, and less transitions to these states from the O 1*s* [6]. Additionally, the more ionic the Fe—O bond is, the more oxygen electrons stay in the 2p state, resulting in less transitions to that state from the O 1*s* state [6]. Thus a higher peak (a) suggests a more covalent bond with more exchange of electrons between the oxygen and iron atoms. The peak (b) relates to the transition from the O 1*s* to the unoccupied hybridized O 2p/Fe 4*s* and 4p states. The relative position of peak (b) compared to (a) relates mainly to the bond length, with a smaller energy difference corresponding to longer bond lengths. Finally, peak (c) corresponds to the coordination of the oxygen atom, since both Fe_3O_4 and γ-Fe_2O_3 contain a mixture of tetrahedral and octahedral coordination while both FeO and α-Fe_2O_3 contain only octahedral configurations. Consequently, the presence of peak (c) suggests a partially tetrahedral configuration.

2. Experimental procedures

2.1. Alloy studied and corrosion experiment

The alloy used for this study was HCM12A, which is a modern ferritic–martensitic alloy. Table 1 shows the elemental composition of this alloy. The samples used in this study were normalized at 1050 °C for 1 h, air-cooled, then tempered for 7 h at 770 °C and air-cooled. This metallurgic process creates alloys with a martensitic lath structure and in which all the carbon in solution has precipitated as $Cr_{23}C_6$ along the lath and prior austenite grain boundaries [11].

The corrosion experiments were performed in the supercritical water corrosion loop at the University of Wisconsin. The supercritical loop is described in more detail in other articles [12,13]. The pressure used was 25 MPa, the temperature was 600 °C and the dissolved oxygen content was ~25 ppb. The sample used for this study was exposed for 2 weeks. Fig. 2 shows a cross-sectional backscattered scanning electron microscopy (SEM) image of the sample, from which a transmission electron microscopy (TEM) sample was prepared using the focused-ion beam (FIB). The location of the FIB sample is shown by a dashed box at the inner-diffusion layer interface.

2.2. Sample preparation and EFTEM/EELS technique

The TEM samples were obtained from 3 mm disk cross-sectional samples using the focused-ion beam (FIB). The preparation of the 3 mm disks is described in previous articles [14,15]. The FIB process enables us to locate a specific area in the oxide layer for study and creates a TEM sample with a relatively large (about 5 μm × 10 μm) area of electron transparency. The samples were prepared using the in situ lift-out procedure [16] using a FEI Quanta 200 3D Dual Beam Focused Ion Beam [17]. The samples were thinned to electron-transparency using an ion beam voltage of 30 kV with the current dropping from 7 nA to 30 pA during the process. Fig. 3 shows a low magnification TEM image of the HCM12A sample analyzed in this article centered on the inner-diffusion layer interface.

The TEM analysis of the sample was performed using a JEOL LaB_6 2010 at 200 kV. The energy filtered imaging (EFTEM) and

Table 1
Elemental composition of HCM12A in wt.%.

Alloy	C	N	Al	Si	P	S	V	Cr	Mn	Fe	Ni	Cu	Nb	Mo	W	Others
HCM12A	.11	.063	.001	.27	.016	.002	.19	10.83	.64	Bal.	.39	1.02	.054	.3	1.89	B: 31 ppm

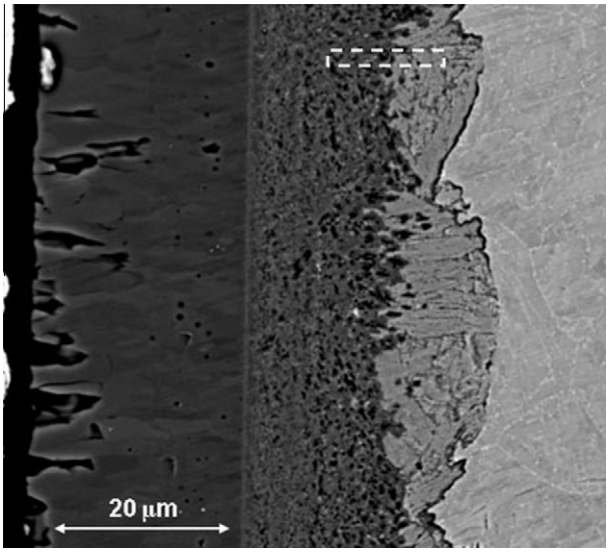

Fig. 2. Cross sectional SEM backscattered image of the oxide formed on HCM12A exposed to 600 °C SCW for 2 weeks.

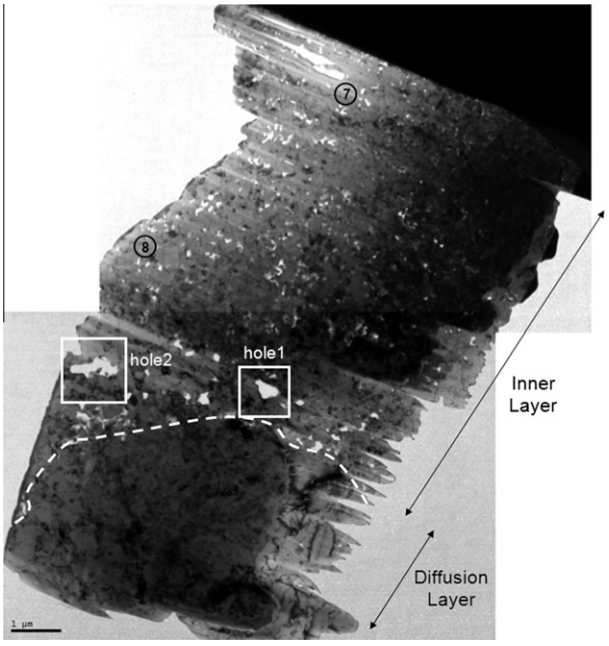

Fig. 3. Low magnification bright-field TEM image of the inner-diffusion layer interface of the HCM12A sample prepared using the FIB. Locations of where EELS spectra were acquired are shown. The dotted white line represents the inner-diffusion layer interface.

electron energy loss spectra (EELS) were obtained on the same microscope equipped with a Gatan Tridiem™ energy filter. Fig. 4 shows a typical EELS spectrum, with the background of the oxygen edge removed, taken from the HCM12A sample and showing the oxygen K edge (532 eV), and the chromium (575 eV) and iron (708 eV) L edges. The iron and oxygen EFTEM maps were obtained by acquiring three images through an energy filter window of ~30 eV for 30 s each: one image taken post-edge and two pre-edge images used for background subtraction. The chromium maps were more difficult to obtain due to the presence of the oxygen edge right before the chromium edge: the energy window was narrowed to ~15 eV and one pre-edge image was taken right before the chromium edge while the other was taken before the oxygen edge.

An EELS spectrum is obtained by bombarding the sample with electrons of constant energy (in our case 200 keV). Some of these electrons lose energy to the sample and others go through with unaltered energy (zero-loss). The amount of energy lost by these electrons depends on the elements present and their crystallographic configuration in the matrix, since each element absorbs the electron's energy at a specific energy, forming an electron energy loss edge. Thus EELS enables the detection of elements by the edge location, and when analyzing the fine structure of this edge can help determine the crystallographic phase and oxidation state of the element. All the EELS spectra were acquired with a resolution of 0.05 eV/channel.

3. Results

The TEM sample used for this study was prepared so that it included both the inner (IL) and the diffusion layer (DL) along with the IL–DL interface. The results are divided into two parts: the first part focuses on the inner layer (IL) and the second on the diffusion layer (DL).

3.1. Analysis of the inner layer

3.1.1. EFTEM analysis

The inner layer contains small equiaxed grains and small pores distributed throughout the layer as was shown in previous articles [3,4,17]. The FIB sample preparation can affect the sample surface during thinning and can create elongated holes in the sample. In this case, only the upper left-hand corner of the sample shown in Fig. 3 appears affected by the FIB process but the other pores were observed using the SEM during the sample preparation process so do not correspond to an artifact. Larger pores are observed right at the IL–DL interface and no pores are seen in the diffusion layer.

The overall grain structure and pore distribution appear uniform throughout the layer, but EFTEM images of this layer reveal an uneven distribution of elements on a nanometric and micrometric scale. Fig. 5 shows the oxygen, iron and chromium maps for most of the inner layer of the sample. While the oxygen level is homogeneous, the levels of iron and chromium are not. The difference of contrast observed in the oxygen map is due to variations in thickness of the sample and not to variations in oxygen content. The iron and chromium maps are complementary, in the sense that chromium-rich regions and depleted in iron and vice versa. These maps highlight the presence of chromium-rich regions that appear to be linked with the pores located in the inner layer since a strong chromium signal is observed around pores and some narrow chromium-rich regions appear to link pores together, as highlighted in the schematic. This suggests that iron migrates preferentially from these areas and that the outward migration of iron forms the pores. Therefore these pores are most likely the result of a coalescence of iron vacancies.

Furthermore, on a smaller scale, in between the chromium-rich regions linked to inner layer porosity, detailed examination shows that the iron and chromium distribution is also not uniform. Fig. 6 shows higher magnification oxygen, chromium and iron EFTEM maps that highlight this nanometric separation of chromium and iron. The small chromium-rich regions are about 100–200 nm in length and about 30 nm in width and appear to be aligned either along the oxide growth direction or perpendicular to it. This elemental segregation is consistent with the presence of both $FeCr_2O_4$ and Fe_3O_4 in the inner layer, as observed from the synchrotron diffraction data presented in previous articles [5,14].

Fig. 7 shows the oxygen, chromium and iron EFTEM maps for the second half of the sample containing the inner-diffusion layer interface and part of the diffusion layer. A more detailed analysis of the

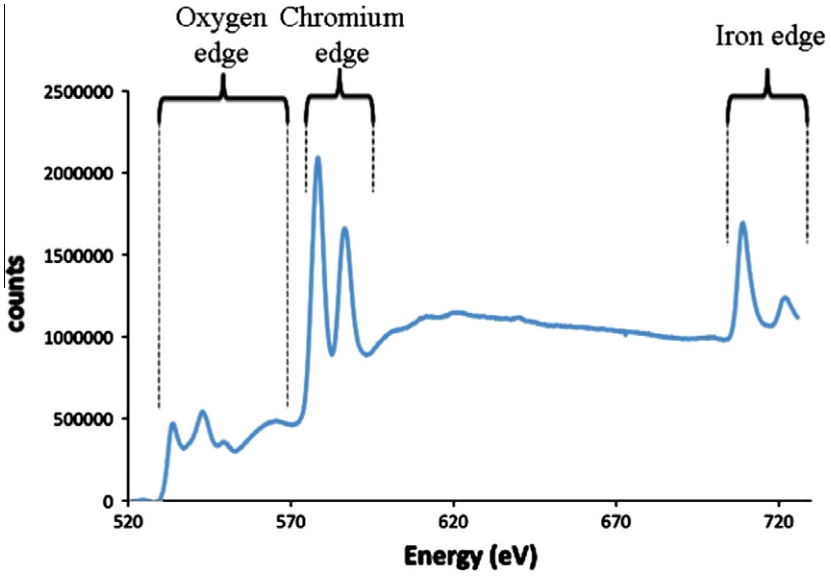

Fig. 4. Typical EELS spectrum, with the oxygen edge background removed, showing the oxygen, chromium and iron edges.

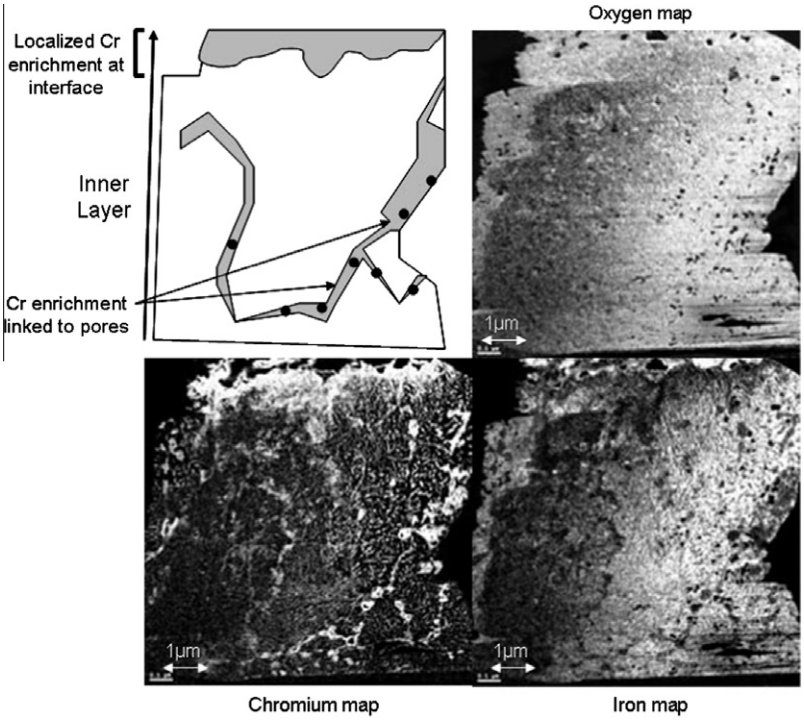

Fig. 5. Oxygen, chromium and iron EFTEM maps for the inner layer of the HCM12A 600 °C 2-week sample.

diffusion layer of this sample is presented in Section 3.2 but we focus here on the interface. Moving from the inner layer to the diffusion layer, we note that this interface is characterized by a chromium-rich region followed by a region depleted in chromium but containing iron and marked with a white dashed-line rectangle in the chromium map of Fig. 7. This is consistent with the synchrotron diffraction data that showed peaks associated with chromium-rich phases such as $FeCr_2O_4$ and a small amount of Cr_2O_3 alongside the FeO peak seen at this interface as was shown in a previous article [5].

3.1.2. EELS analysis

The EFTEM maps were used to locate areas of interest for the EELS analysis, which consisted of the comparison of phases in chromium rich and iron rich regions. These areas were mainly located right at the IL–DL interface designated as *hole 1* (spectra 1–3) and *hole 2* (spectra 4–5) in Fig. 3 and the EELS spectra obtained should be compared to the ones obtained by Colliex et al. shown in Fig. 1 [6]. A few additional spectra (spectra 7 and 8) were acquired from further inside the inner layer.

Fig. 8 shows the *hole 1* region with chromium, iron and oxygen EFTEM maps (the spectra locations are marked in the chromium map), and three of the oxygen edge spectra: spectrum 1 (defective Fe_3O_4), spectrum 2 (Fe_3O_4), and spectrum 3 ($FeCr_2O_4$). Fig. 9 shows the EFTEM maps and three spectra for the *hole 2* region: spectrum 4 (Cr_2O_3), spectrum 5 (defective Fe_3O_4), and spectrum 6 (Fe_3O_4). Finally, Fig. 10 shows spectrum 7 (close to FeO) and spectrum 8

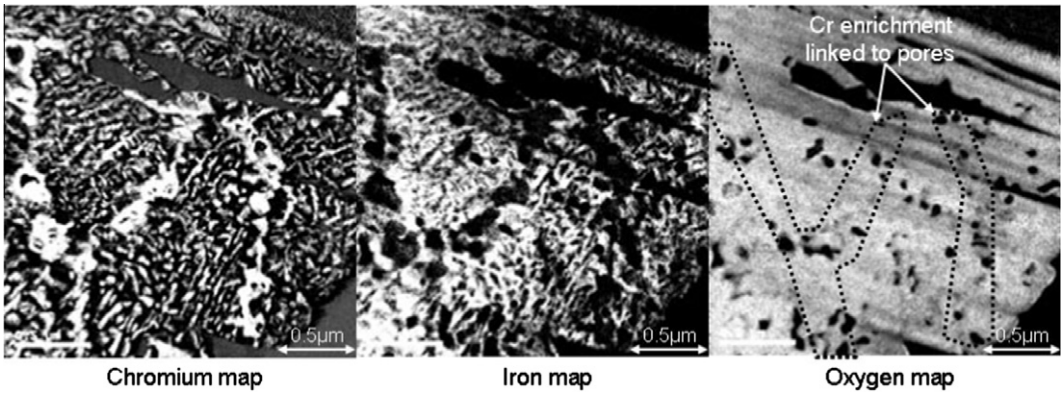

Fig. 6. Chromium, iron and oxygen EFTEM maps of the middle of the inner layer of the HCM12A 600°C 2-week sample showing the nanometric Fe–Cr separation.

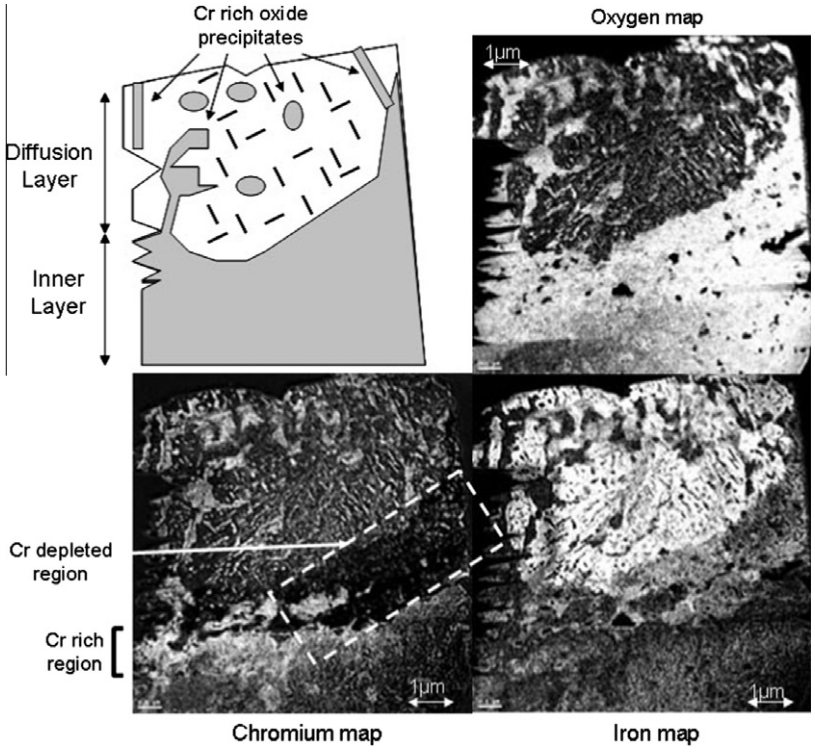

Fig. 7. Oxygen, chromium and iron EFTEM maps for the inner-diffusion layer interface and part of the diffusion layer of the HCM12A 600 °C 2-week sample.

(defective Fe_3O_4) taken further in the inner layer as seen in Fig. 3.

The regions containing no chromium resulted in spectra with characteristics corresponding to the spectrum of Fe_3O_4 with a distinctive peak (c), a narrow peak (a) with an amplitude near half that of peak (b), and narrow peak (d). Nevertheless, some small differences were observed enabling the distinction between defective Fe_3O_4 (containing a higher Fe^{2+} to Fe^{3+} ratio compared to stoichiometric Fe_3O_4) and Fe_3O_4. The average amplitude of peak (a) relative to peak (b) was measured for the different spectra and resulted in an average value of 0.68 for the stoichiometric Fe_3O_4 spectra (spectra 2 and 6), in agreement with the values found in the literature [6,10]. For these same spectra, the average peak (b) to peak (a) energy difference is of 9.78 eV. In contrast, the defective Fe_3O_4 spectra have an average amplitude ratio of 0.63 and an average peak energy difference of 9.61 eV. The defective Fe_3O_4 contains a higher fraction of Fe^{2+}, which contains more 3d electrons than Fe^{3+}, resulting in less unoccupied O 2p/Fe 3d states and thus a lower peak (a). The Fe—O bond is overall larger in FeO than in Fe_3O_4, suggesting larger Fe—O bonds when Fe^{2+} is involved (in agreement with the increasing energy difference from FeO to Fe_2O_3).

The spectra containing both iron and chromium with a chromium to iron ratio near 3 (such as spectrum 3) are quite different from the Fe_3O_4 spectra showing a relatively high amplitude ratio between peak (a) and (b). This ratio is equal to 0.89 on average and the peak energy difference is around 9.41 eV. The high amplitude ratio is due to the electron configuration of chromium, which contains two electrons less in the 3d band when oxidized, compared to Fe^{3+}. Consequently, there are more unoccupied O 2p/Fe 3d states for the O 1*s* transition entailing a more intense peak (a). Concerning the lower energy difference, as the Cr replaces iron in the octahedral sites, it pushes the Fe^{2+} ions into the tetrahedral sites, which expands the unit cell to accommodate the larger Fe^{2+} ion, making the Fe—O bonds larger. Additionally, chromium has a

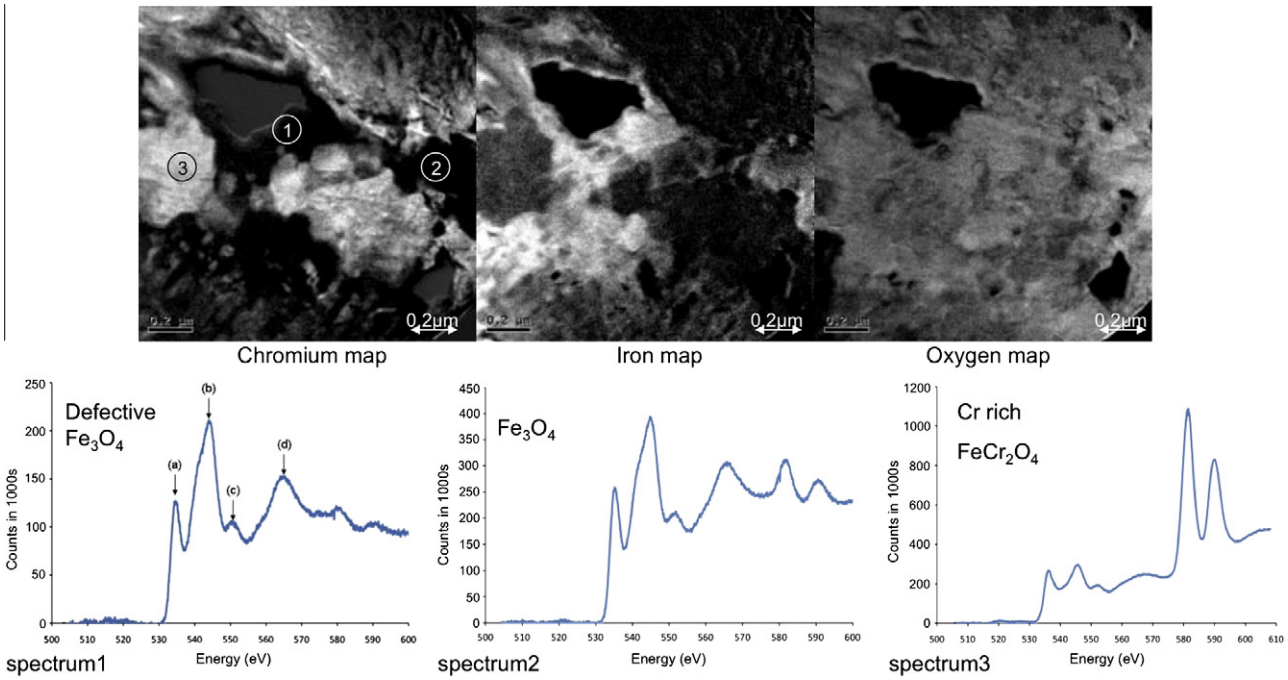

Fig. 8. Cr, Fe, and O EFTEM maps from *hole 1* region and corresponding EELS spectra.

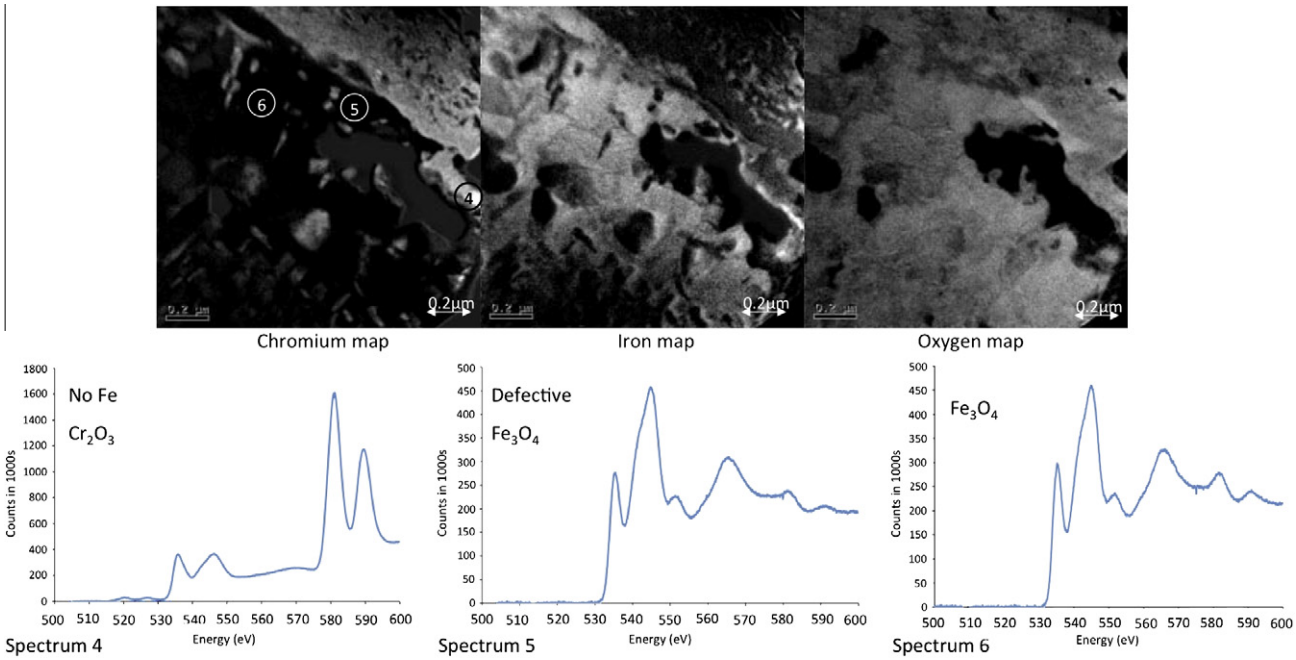

Fig. 9. Cr, Fe, and O EFTEM maps from *hole 2* region and corresponding EELS spectra.

smaller radius that iron in the octahedral site. Therefore the overall bond length with the cations from the oxygen point of view is longer than the bond lengths in Fe_3O_4.

Spectrum 4 contains almost only chromium with a chromium to iron ratio close to 6, which may be associated with a Cr_2O_3 phase containing a small amount of iron. The spectrum differs from the other chromium-rich spectra, showing a large energy difference between peak (b) and peak (a), and an amplitude ratio close to 1. The amplitude ratio is 0.955, which is much higher than for other spectra. This is due to the absence of Fe^{2+}, and thus more unoccupied hybridized O 2p/Fe 3d states. The energy difference is 10.38 eV, once again much larger than for all the other spectra, and close to the value corresponding to Fe_2O_3 presented by Colliex et al. [6]. This greater energy difference suggests an increased covalency of the Cr—O bond and a shorter bond length of the oxygen atom with the neighboring cations. Catti et al. have shown that the Cr—O bond in Cr_2O_3 is more covalent than the Fe—O bond in Fe_2O_3 with an electron transfer of about $0.675|e|$ for Cr_2O_3 and only $0.382|e|$ for Fe_2O_3 [18]. As described by Colliex et al., when the amount of Fe^{2+} decreases, the energy difference between peak (a) and (b) increases due to shorter bond lengths so it is normal to observe such an increase if the probed area is Cr_2O_3 [6].

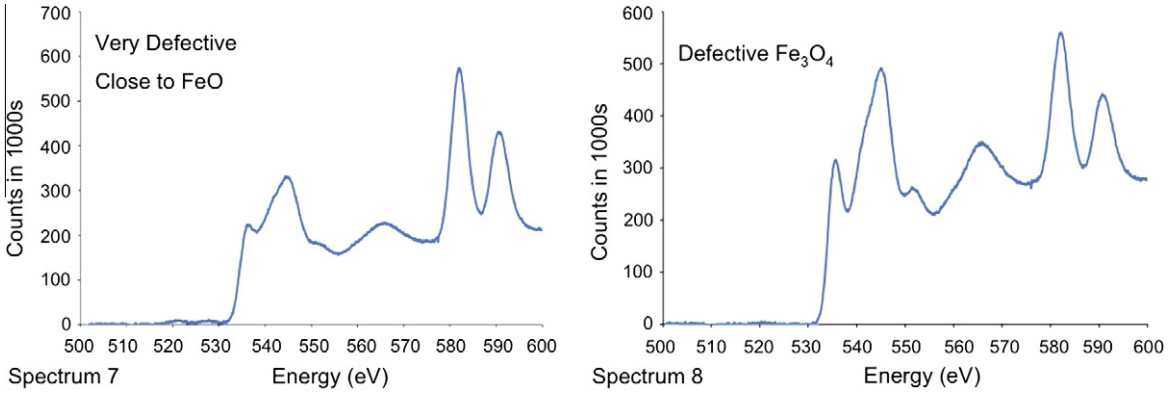

Fig. 10. Oxygen edge spectra in different areas further into the inner layer.

Finally, spectra 7 and 8 taken further into the inner layer are from iron-rich areas containing chromium-to-iron ratios of 0.6 and 0.3, respectively. Spectrum 8 corresponds to a defective Fe_3O_4 spectrum with the presence of a relatively strong peak (c), a peak (a) to (b) amplitude ratio of 0.64 and an energy difference of 9.38 eV. Consequently, it exhibits similar features to spectra 1 and 3 for example, corresponding to a Fe_3O_4 structure containing a higher Fe^{2+} ratio and therefore longer Fe—O bonds, and so a shorter energy difference. Spectrum 7 shows different features compared to the rest of the spectra studied for this alloy since its peak (a) to (b) amplitude ratio is 0.6 and its energy difference is 8.65 eV, both of which are much smaller than for other spectra. These characteristics are similar to those shown for FeO in the article by Colliex et al. [6], which suggests that this spectrum could be associated with FeO. The spectrum is indeed similar to the one for FeO displayed in Fig. 1, containing almost no peak (c) as would be expected for the totally octahedral symmetry found in FeO. This reinforces the conclusion that FeO is present in the layer, confirming in the synchrotron diffraction data.

3.2. Analysis of the diffusion layer

A previous article had shown that in the diffusion layer oxide precipitates preferentially formed along the tempered martensite lath boundaries where chromium carbides are present in the base alloy [5]. Fig. 11 shows an SEM backscattered image of the diffusion layer of the HCM12A 600 °C 2-week sample exhibiting the preferential oxidation along the lath boundaries. In this Figure, the oxide precipitates are oriented according to the orientation of the laths present in the base metal. This shows the influence on the oxidation process of the base metal microstructure, which is outlined by the white chromium carbides. These large micrometric precipitates correspond to the chromium-rich oxides present near the edges of the sample in the EFTEM image of Fig. 7.

The iron rich region in the center of Fig. 7 corresponds to a metal grain outlined by the large chromium rich precipitates on either side. This region is characterized by a nanometric iron–chromium segregation forming small chromium-rich oxide precipitates about 10 nm in width and 100–200 nm in length. Fig. 12 shows a close-up of these precipitates using EFTEM chromium, iron and oxygen maps. The nanometric precipitates are aligned perpendicular to each other.

These precipitates were analyzed using selected area electron diffraction in the TEM. Fig. 13 shows the highly-ordered [001] Fe-bcc and [011] spinel diffraction patterns with a corresponding dark-field image outlining the small nanometric spinel oxide precipitates. The dark-field image clearly shows the elongated chromium-rich oxide particles observed previously using EFTEM. Since these particles were seen to be chromium-rich in the elemental EFTEM mapping, the spinel phase is most likely $FeCr_2O_4$. Consequently, the diffusion layer consists of a mixture of chromium-rich oxide precipitates forming along the grain and lath boundaries, and metal grains containing within them much smaller $FeCr_2O_4$ particles aligned perpendicularly one to another and with a well defined orientation relationship with the bcc iron matrix. This orientation relationship appears to be the Baker–Nutting orientation relationship typical of fcc particles in a bcc matrix: $\{001\}_{spinel}//\{001\}_{bcc}$ and $<100>_{spinel}//<110>_{bcc}$, which leads to the formation of square-shaped plates due to a large misfit along the $[001]_{spinel}//[001]_{bcc}$. The formation of these plates would explain the rectangular shape of the particles observed in the TEM images.

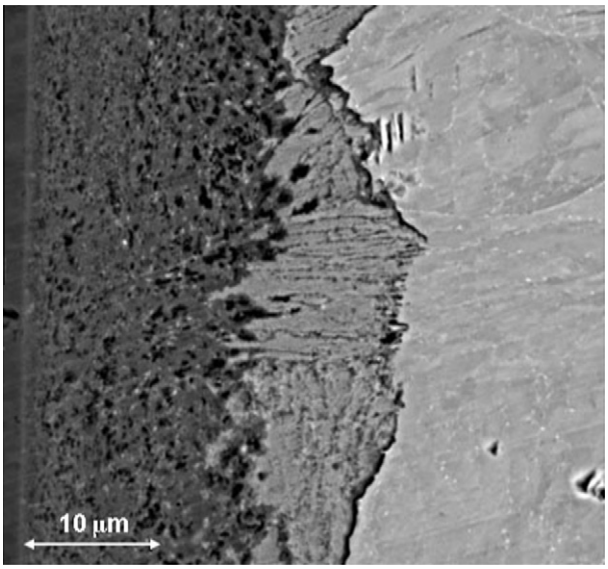

Fig. 11. SEM backscattered image of the diffusion layer of the HCM12A 600 °C 2-week sample.

These observations are consistent with a mechanism of oxide advancement in two steps: firstly phase separation occurs in the diffusion layer during the formation of small $FeCr_2O_4$ precipitates within the metal grain (iron–chromium segregation due to negligible solubility of oxygen in iron [19,20]), and secondly the remaining iron surrounding these particles oxidizes to form a mixture of Fe_3O_4 and $FeCr_2O_4$ when the inner layer advances in the diffusion layer.

4. Discussion

The results shown above give some insight on the advancement of the oxide front and the formation of the diffusion layer. The

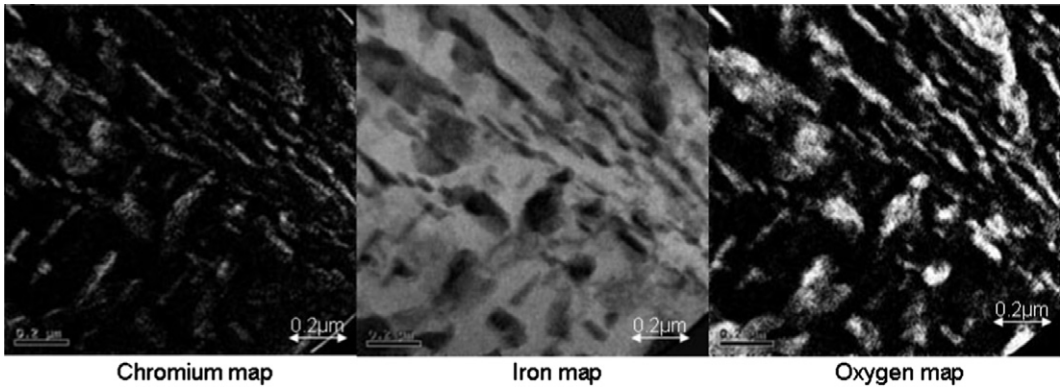

Fig. 12. Close-up of the nanometric chromium-rich oxide precipitates using EFTEM chromium, iron and oxygen maps.

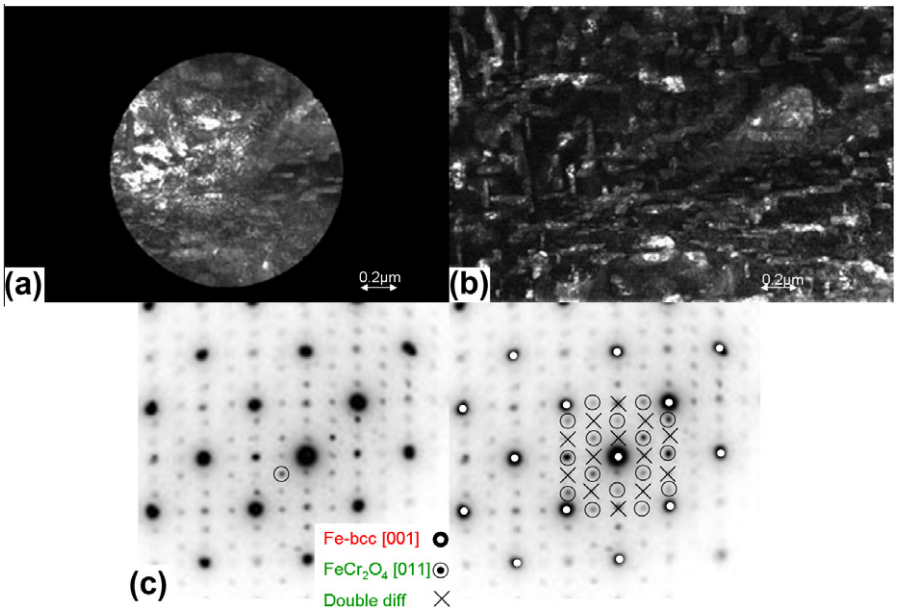

Fig. 13. Highly ordered [001] Fe-bcc and [011] spinel patterns (c) with corresponding (a) bright-field and (b) dark-field images taken with a spot from the spinel pattern (circled).

oxide in the diffusion layer forms preferentially along the tempered martensite lath boundaries, which suggests that the oxygen diffuses primarily through these boundaries. This is how the oxygen permeates the metal and therefore the oxidation process is influenced by the base metal microstructure. Previous studies have suggested that the rate-limiting step in the corrosion of ferritic–martensitic alloys in SCW is the outward diffusion of iron and not the diffusion of oxygen [2,21,22]. This is consistent with the presence of the diffusion layer observed in these samples and the lath boundaries provide an extensive network of short-circuit diffusion paths for the oxygen, which quickly diffuses to the oxide-metal interface. The chromium carbides along these lath boundaries are oxidized to form chromium-rich oxides such as Cr_2O_3 or $FeCr_2O_4$ present in the diffusion layer [14,21].

Fig. 14 shows a schematic of the advancement of the inner layer into the diffusion layer. Once the oxygen has diffused along the lath boundaries, and surrounds the metal grains, it begins to diffuse inside this metal grain. Since the oxygen solubility in iron is negligible [19,20], this forces an iron–chromium segregation through the formation of nanometric chromium-rich spinel oxides. The oxygen potential being low, only chromium-rich oxides can form [2,4,19,20]. As more of these small oxide particles form within the metal grain, the oxygen potential within the metal grain increases until it reaches the critical oxygen level necessary to form Fe_3O_4. At this point the iron present in the rest of the metal grain becomes oxidized, which constitutes the advancement of the inner layer into the diffusion layer. This creates an iron-rich region right at the inner-diffusion layer interface as observed in Fig. 7. This newly oxidized iron will then diffuse outwards to form the outer layer, enriching the new inner-diffusion layer interface in the process, and going through the previous chromium-rich inner-diffusion layer interface, which will thus disappear. The presence of additional oxidized iron locally leads to more iron-rich spinel oxide, which is consistent with the EELS analysis showing the presence of defective Fe_3O_4 containing a slight excess of Fe^{2+}. Additionally, the oxidized chromium present in the nanometric chromium-rich spinel oxides diffuse very slowly compared to iron and chromium stabilizes the spinel structure by its presence in the octahedral sites of the structure [23–27]. Consequently, chromium will undergo minimal diffusion once it is oxidized, which could explain the presence of the small nanometric chromium–iron elemental separation observed in the inner layer linked with the formation

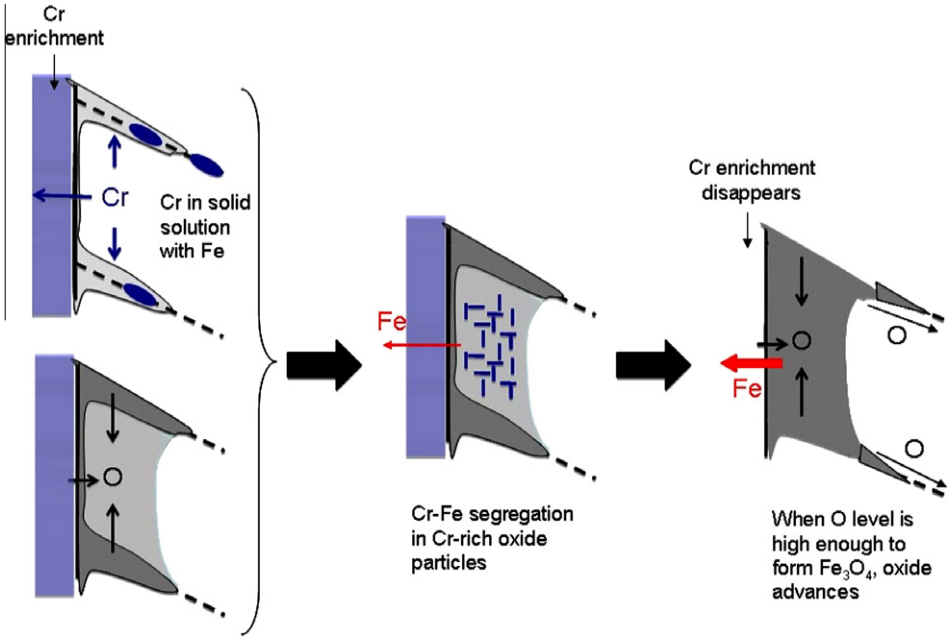

Fig. 14. Schematic of the advancement of the inner layer into the diffusion layer.

of the small spinel precipitates within metal grains in the diffusion layer. The size and orientation of these precipitates is consistent in both layers.

With this in mind, it is interesting to investigate the influence of the diffusion layer on the oxidation behavior of ferritic–martensitic alloys. For example, ODS steels corrode at a lower rate than conventional ferritic–martensitic steels and exhibit a much thicker diffusion layer [28–31]. When comparing the weight gain in SCW of the 9CrODS alloy (9 wt.% Cr) compared to that of NF616 (9 wt.% Cr) and HCM12A (12 wt.% Cr), the 9CrODS steel showed a lower weight gain than that of the two other alloys even though it contained less chromium than HCM12A for example [29,30]. Additionally, the ODS alloys form more and larger chromium-rich oxide precipitates (especially Cr_2O_3) in the diffusion layer, which can affect the corrosion behavior [29,30]. This suggests that a thicker and more chromium-rich diffusion layer leads to slower corrosion, thus showing the importance of this layer in the corrosion process. This influence on the oxidation behavior can be explained by the presence of large chromium-rich precipitates located at lath boundaries, which slow down the outward iron diffusion by preventing grain boundary diffusion. Additionally, most of the oxygen in the diffusion layer is used to oxidize chromium, therefore limiting the amount of oxidized iron that will diffuse outward to form the outer layer.

5. Conclusions

The advancement of the oxide front was analyzed through the TEM investigation of the inner-diffusion layer interface of an HCM12A sample oxidized in 600 °C SCW for 2 weeks. The EFTEM and EELS analysis of this sample led to the following conclusions concerning the understanding of the corrosion process of ferritic–martensitic alloys:

1. The inner layer contains chromium-rich zones linked with the porosity suggesting that the pores originate from the outward migration of iron.
2. A nanometric iron–chromium elemental separation is observed in the inner layer, which could be associated with the presence of both Fe_3O_4 and $FeCr_2O_4$.
3. The EELS analysis showed the presence of defective Fe_3O_4 containing an excess of Fe^{2+} near the inner-diffusion layer interface, which may be associated with the advancement of the inner layer into the diffusion layer.
4. The diffusion layer is characterized by the presence of large chromium-rich oxide precipitates along the tempered martensite lath boundaries due to the preferential grain boundary diffusion of oxygen. The chromium carbides present at these boundaries are oxidized to form the chromium-rich oxides.
5. As oxygen diffuses within the metal grain, small nanometric chromium-rich oxide precipitates (mainly $FeCr_2O_4$) form due to the negligible solubility of oxygen in iron. These precipitates may be associated with the iron–chromium separation observed in the inner layer.

Consequently, both the inner and the diffusion layers exhibit a complex structure with a non-uniform distribution of elements. The results give some insight on the corrosion mechanism and especially on the advancement of the inner layer into the diffusion layer. It appears that the diffusion layer plays an active role in slowing down the outward diffusion of iron ions and therefore influences the corrosion behavior of these alloys.

Acknowledgments

The authors would like to thank Trevor Clark and Joe Kulik for their help in the TEM sample preparation and examination. This publication was supported by the Pennsylvania State University Materials Research Institute Nanofabrication Lab and the National Science Foundation Cooperative Agreement No. 0335765, National Nanotechnology Infrastructure Network, with Cornell University. This study was funded by DOE-NERI Project DE-FC07-06ID14744.

References

[1] Report A Technology Roadmap for Generation IV Nuclear Energy Systems, GIF-002-00, 2002.
[2] L. Tan, M.T. Machut, K. Sridharan, T.R. Allen, J. Nucl. Mater. 371 (2007) 161–170.
[3] L. Tan, Y. Yang, T.R. Allen, Corros. Sci. 48 (2006) 4234–4242.
[4] L. Tan, Y. Yang, T.R. Allen, Corros. Sci. 48 (2006) 3123–3138.

[5] J. Bischoff, A.T. Motta, L. Tan, T.R. Allen, in: Materials for Future Fusion and Fission Technologies, 2–4 December 2008, vol. 1125, USA, Materials Research Society, Warrendale, PA, 2009. pp. 19–24.
[6] C. Colliex, T. Manoubi, C. Ortiz, Phys. Rev. B (Condens. Matter) 44 (1991) 11402–11411.
[7] J. Jasinski, K.E. Pinkerton, I.M. Kennedy, V.J. Leppert, Microsc. Microanal. 12 (2006) 424–431.
[8] T. Manoubi, M. Tence, M.G. Walls, C. Colliex, Microanal., Microstruct. 1 (1990) 23–39.
[9] C. Mitterbauer, G. Kothleitner, W. Grogger, H. Zandbergen, B. Freitag, P. Tiemeijer, F. Hofer, in: International Workshop on Strategies and Advances in Atomic Level Spectroscopy and Analysis (SALSA), 5–9 May 2002, vol. 96, Elsevier, Netherlands, 2003. pp. 469–480.
[10] C. Wang, D.R. Baer, J.E. Amonette, M.H. Engelhard, J. Antony, Y. Qiang, J. Am. Chem. Soc. 131 (2009) 8824–8832.
[11] R.L. Klueh, D.R. Harries, High Chromium Ferritic and Martensitic Steels for Nuclear Applications, ASTM, West Conshohocken, PA, 2001.
[12] K. Sridharan, S.P. Harrington, A.K. Johnson, J.R. Licht, M.H. Anderson, T.R. Allen, Mater. Des. 28 (2007) 1177–1185.
[13] K. Sridharan, A. Zillmer, J.R. Licht, T.R. Allen, M.H. Anderson, L. Tan, in: Proceedings of ICAPP 04, Pittsburgh, PA, 2004. pp. 537.
[14] J. Bischoff, A.T. Motta, R.J. Comstock, J. Nucl. Mater. 392 (2009) 272–279.
[15] A. Yilmazbayhan, A.T. Motta, R.J. Comstock, G.P. Sabol, B. Lai, Z. Cai, J. Nucl. Mater. 324 (2004) 6–22.
[16] L.A. Giannuzzi, F.A. Stevie, Micron 30 (1999) 197–204.
[17] A.D. Siwy, T.E. Clark, A.T. Motta, J. Nucl. Mater. 392 (2009) 280–285.
[18] M. Catti, G. Sandrone, G. Valerio, R. Dovesi, J. Phys. Chem. Solids 57 (1996) 1735–1741.
[19] A.R. Setiawan, M. Hanafi Bin Ani, M. Ueda, K. Kawamura, T. Maruyama, Iron Steel Inst. Jpn. (ISIJ) Int. 50 (2010) 259–263.
[20] D.E.J. Talbot, J.D.R. Talbot, Corrosion Science and Technology, CRC Press, Taylor & Francis Group LLC, 2007.
[21] J. Bischoff, A.T. Motta, C. Eichfeld, R.J. Comstock, G. Cao, T.R. Allen, J. Nucl. Mater. submitted for publication.
[22] L. Tan, X. Ren, T.R. Allen, Corros. Sci. 52 (2010) 1520–1528.
[23] J. Topfer, S. Aggarwal, R. Dieckmann, Solid State Ionics 81 (1995) 251–266.
[24] R. Dieckmann, Berichte der Bunsengesellschaft/Phys. Chem. Chem. Phys. 86 (1982) 112–118.
[25] R. Dieckmann, H. Schmalzried, Berichte der Bunsengesellschaft/Phys. Chem. Chem. Phys. 81 (1977) 414–419.
[26] B. Gillot, J.-F. Ferriot, G. Dupré, A. Rousset, Mater. Res. Bull. 11 (1976) 843–849.
[27] Z. Tokei, K. Hennesen, H. Viefhaus, H.J. Grabke, Mater. Sci. Technol. 16 (2000) 1129–1138.
[28] J. Bischoff, A.T. Motta, in: 15th Environmental Degradation of Materials In Nuclear Power Systems 2011, Colorado Springs, 2011.
[29] J. Bischoff, A.T. Motta, J. Nucl. Mater. 424 (2012) 261–276.
[30] J. Bischoff, A.T. Motta, X. Ren, T.R. Allen, in: Proceedings of the 14th Environmental Degradation of Materials In Nuclear Power Systems 2009, American Nuclear Society, 2009, pp. 1764–1770.
[31] Y. Chen, K. Sridharan, S. Ukai, T.R. Allen, J. Nucl. Mater. 371 (2007) 118–128.